Supplementary Methods

MD simulation

As described in [1], the MD simulation of α-synuclein was performed using the Amber12 force field with the TIP4P-D water model. The simulation started from an extended conformation of α-synculein, solvated in an ~ 100 × 100 × 100 Å^3 box containing ~ 40000 water molecules and 0.1 M NaCl. The system was initially equilibrated at 300 K and 1 bar for 1 ns, then production run at 300 K and 1 bar was performed in the NPT ensemble with the Anton specialized hardware at 2.5 fs time step. Nonbonded interactions were truncated at 12 Å and the Gaussian split Ewald method with a 64 × 64 × 64 Å mesh was used to account for the long-range part of the electrostatic interactions. The MD frames were saved at 10 ps intervals.

MD-based autocorrelation functions

Second-order orientational autocorrelation functions (ACF) between nuclei *A* and *B* (H-H for proton relaxometry or N-H for nitrogen relaxation) were calculated from the MD trajectory as [2]:

$$C(t) = \frac{1}{C_0} < \frac{D_{q,0}^{(2)*}(\Omega_0)}{r_0^3} \frac{D_{q,0}^{(2)*}(\Omega_t)}{r_t^3} > \qquad \text{(eq. S1)}$$

where $D_{q,0}^{(2)}(\Omega)$ are the elements of the Wigner rotation matrix, <…> means ensemble averaging, the asterisk means complex conjugation, C_0 is the normalization constant (equal to $C(0)$), Ωs are different sets of Euler angles specifying the orientation of the *AB* vector with respect to the laboratory coordinate frame, *r* is the *AB* distance, and subscripted 0 and *t* denote the initial and final time moments at which *r* and Ω are calculated. To calculate spin relaxation rates, the relevant H-H or N-H ACFs were converted to spectral density functions through Fourier transformations. An exponential window function with a correlation time of 200 ns was applied to all ACFs to ensure that the artificially long components of motions in the MD trajectory do not affect the spectral density functions at very low frequencies. The ACFs were also fitted to multi-exponential decay functions,

$$C(t) = \sum_i S_i^2 \exp(-\frac{t}{\tau_i}) \text{ (eq. S2)}$$

with i= 1, 2, 3, 4, 5 or 6, where S^2_i and τ_i represented the squared order parameters and correlation times corresponding to different motions, respectively, and $\sum S_i^2 = 1$. To evaluate the noise level in the ACFs, the MD trajectory was split into three (non-overlapping) sub-trajectories, each of 5 μs duration, and the ACFs were calculated separately for each sub-trajectory. The standard deviation between the three ACFs represented the noise level in the ACF of the whole trajectory.

Simulated proton relaxometry profiles

Fourier transformation of each pair of inter-proton ACFs provided individual spectral densities at different frequencies. The first 2-μs of the H-H ACFs were taken for Fourier transformation, as a result, spectral densities from 0 to 50 GHz at 0.5 MHz intervals were obtained. R_1 of all non-exchangeable CH_3, CH_2 and CH^α protons were then calculated from the spectral densities, $J(\omega)$, through the equation ,

$$R_1(\omega) = \frac{3}{2} (\frac{\mu_0}{4\pi})^2 \frac{\hbar^2 \gamma_H^4}{r^6} [0.2J(\omega) + 0.8J(2\omega)] \qquad \text{(eq. S3)}$$

in which $J(\omega) = \frac{\tau_R}{1+\omega_H^2 \tau_R^2}$. The magnetization decay functions of all CH_3, CH_2 and CH^α protons were then simulated as:

$$M(t) = M_0 \exp(-R_1 t) \qquad \text{(eq. S4)}$$

for t ranging from 0 to 1 s, and then the collective (experimentally detectable) magnetization decay function M_c was obtained from the average of magnetization decays of all protons. Finally, M_c was fitted with a double exponential decay function,

$$M_c(t) = M_0\ (w_a \exp(-R_a t) + w_b \exp(-R_b t)) + M_{hf} \qquad \text{(eq. S5a)}$$

as it was done for the experimental data [3] (the fit was in all cases very good, with a reduced χ^2 of about 10^{-5}), and the collective relaxation rate was defined as:

$$\langle R_1 \rangle = w_a R_a + w_b R_b \qquad \text{(eq. S5b)}$$

where w_a, R_a, R_b and M_{hf} were fitting parameters (w_b=1- w_a). The calculations were repeated for proton Larmor frequencies of 0.1, 0.5, 1, 2, 3, 5, 10, 15, 20 30 and 50, corresponding to the range of available experimental data [3]. For R_1 calculation at ω=0.1 MHz, J(0.1MHz) and J(0.2MHz) were approximated by J(0). The resulting R_1 dispersion profile was then fitted to the following equation:

$$\langle R_1 \rangle = S_c^2\ \langle E^2 \rangle \left(\frac{0.2\tau_R}{1+\omega_H^2\tau_R^2} + \frac{0.8\tau_R}{1+4\omega_H^2\tau_R^2} \right) + \alpha \quad \text{(eq. S6a)}$$

which includes a single correlation time, or

$$\langle R_1 \rangle = \langle E^2 \rangle\ [S_{c(1)}^2 \left(\frac{0.2\tau_{R1}}{1+\omega_H^2\tau_{R1}^2} + \frac{0.8\tau_{R1}}{1+4\omega_H^2\tau_{R1}^2} \right) + S_{c(2)}^2 \left(\frac{0.2\tau_{R2}}{1+\omega_H^2\tau_{R2}^2} + \frac{0.8\tau_{R2}}{1+4\omega_H^2\tau_{R2}^2} \right)] + \alpha \text{ (eq. S6b)}$$

with two correlation times. The $\langle E^2 \rangle$ was fixed to 2.4×10^{10} s^{-2}, as previously calculated with CORMA [3-4].

Simulated ^{15}N relaxation rates

Second-order orientational ACFs for the 134 individual backbone N-H vectors of α-synuclein (all residues except M1 and prolines 108, 117, 120, 128 and 138) were calculated from the MD trajectory. Next, individual ACFs were converted to spectral density functions at different frequencies through Fourier transformation, as described above. Only the first 30-ns of the N-H ACFs, during which the ACFs generally decayed below 0.5% of the initial value, were taken for Fourier transformation. Then, ^{15}N longitudinal (R_1) and transverse (R_2) auto-relaxation rates and transverse cross-correlated relaxation rates (*CCR,* η_{xy}) were calculated as:

$$R_1 = \left(\frac{d^2}{4}\right)[J(\omega_H - \omega_N) + 3J(\omega_N) + 6J(\omega_H + \omega_N)] + c^2 J(\omega_N) \qquad \text{(eq. S7a)}$$

$$R_2 = \left(\frac{d^2}{8}\right)[4J(0) + J(\omega_H - \omega_N) + 3J(\omega_N) + 6J(\omega_H) + 6J(\omega_H + \omega_N)] + \left(\frac{c^2}{6}\right)[4J(0) + 3J(\omega_N)]$$

(eq. S7b)

$$\eta_{xy} = \frac{\sqrt{3}}{6} c d P_2(cos\theta)[4J(0) + 3J(\omega_N)] \text{ (eq. S7c)}$$

where $d = -\frac{\mu_0 \hbar \gamma_H \gamma_N}{4\pi r_{NH}^3}$ and $c = \frac{\gamma_N \Delta\sigma\, B_0}{\sqrt{3}}$. The effective NH bond length of 1.04 Å was used to account for zero-point vibrations [5] and the ^{15}N CSA tensor magnitudes ($\Delta\sigma$) were set to -170 ppm. The angle θ between NH bond vectors and the main axis of the ^{15}N CSA tensors was set to 22.5° [6]. To optimize the scaling factors for the correlation times and/or the order parameters corresponding to different motions present in the MD-derived N-H ACFs, the spectral density functions at angular frequency ω were first calculated using the best-fit parameters obtained with three-exponential decay function as:

$$J(\omega) = \frac{2}{5}\ (S_{slow}^2 \frac{\tau_{slow}}{1+(\omega.\tau_{slow})^2} + S_{int}^2 \frac{\tau_{int}}{1+(\omega.\tau_{int})^2} + S_{fast}^2 \frac{\tau_{fast}}{1+(\omega.\tau_{fast})^2}) \qquad \text{(eq. S8)}$$

and subsequently the relaxation rates R_1 and R_2 were predicted through equations 7a-b. The optimal temporal and order parameter scaling factors were then obtained through minimization of the relative root mean square of deviation (rmsd) between the experimental and predicted relaxation rates, as:

$$rmsd = sqrt[(\left(\frac{R_{1,pred}-R_{1,exp}}{R_{1,exp}}\right))^2 + \left(\frac{R_{2,pred}-R_{2,exp}}{R_{2,exp}}\right))^2/2] \text{ (eq. S9)}$$

Experimental ^{15}N relaxation rates

^{15}N R_1 and R_2 rates, ^{1}H,^{15}N heteronuclear NOE and transverse cross-correlated relaxation rates (*CCR,* η_{xy}) of α-synuclein were measured at a proton Larmor frequency of 600 MHz (and in case of R_2, also at 800 MHz) using AVANCE-III Bruker (Karlsruhe, Germany) spectrometers. The uniformly ^{15}N-labeled NMR sample contained ~ 1 mM α-synuclein at pH 5.0 dissolved in 10% D_2O/90% H_2O. The temperature was set to 25 °C. The pH and temperature were identical to those used for experimental proton relaxometry experiments [3]. ^{15}N R_1 rates were measured using conventional pulse sequence schemes with ten relaxation delays between 10 and 1000 ms [7]. ^{15}N R_2 rates were obtained using a CPMG-based scheme with a τ_{cp} of 1 ms and relaxation delays of 12, 32, 52, 72, 92, 112, 132, 152 and 172 ms [7]. R_1 and R_2 relaxation rates were determined by fitting the corresponding peak intensities to a single exponential decaying function. Errors in relaxation rates were estimated from 500 Monte Carlo (MC) simulation runs for which the fit residuals were taken as the random noise. Steady-state hetNOEs were obtained by comparison of peak intensities between saturated and reference spectra, where the duration of saturation block and the total recycle delay in the hetNOE were 5 and 8 s, respectively. The R_1, R_2 and hetNOE measurements were performed in FID-interleaved manner. The *CCR* rates were measured using relaxation delays of 100, 150 and 200 ms [8]. The exchange-free R_2 rates, R_2^0, were derived from *CCR* as described in [9]. Reduced spectral density mapping analysis of ^{15}N relaxation rates [10] was made using an in-house MATLAB script.

Single-molecule fluorescence spectroscopy

Labeling of α-synuclein with Alexa Fluor 488 and 594 for single-molecule FRET measurements. A double-cysteine variant of α-synuclein (S42C and T92C) was reduced with 1,4-Dithiothreitol (DTT) and subsequently purified by RP-HPLC using a Reprosil Gold C18 column with a water-acetonitrile (ACN) gradient (Solvent A: 0.1% TFA, Solvent B: ACN; gradient: 5-50% B in 30 min). The protein was labeled with the donor dye Alexa Fluor 488 maleimide in 6 M guanidinium chloride (GdmCl), 100 mM sodium phosphate, pH 7.3, overnight at 4°C at a molar ratio of dye to protein of 0.7:1. The reaction was stopped by adding DTT. A gradient of 37-42% B over 30 min was chosen to separate unlabeled, singly and doubly donor-labeled protein on the Reprosil Gold C18 column. Singly labeled material was further labeled with the acceptor dye Alexa Fluor 594 maleimide at a molar ratio of dye to protein of 5:1 for 4 h at room temperature. Unreacted dye was quenched with DTT. Purification of donor-acceptor labeled protein was achieved by RP-HPLC as described above. The mass of donor/acceptor-labelled α-synuclein was confirmed by ESI-MS.

Single-molecule fluorescence spectroscopy.

Single-molecule fluorescence measurements were conducted on a MicroTime 200 confocal microscope (PicoQuant, Germany). Labeled molecules were excited with a diode laser (LDH-D-C-485, PicoQuant, Germany) in continuous-wave mode. Emitted fluorescence was collected by the objective (UplanApo 60x/1.20W, Olympus) and filtered (HQ500LP, Chroma Technology) before passing the confocal pinhole (100 μm diameter). The emitted photons were then sorted into four channels, first by a polarizing beam splitter and then by a dichroic mirror (585DCXR, Chroma) for each polarization. Donor and acceptor emission was filtered (ET525/50m or HQ650/100m, respectively, Chroma Technology) and then focused

on a τ-SPAD avalanche photodiode (PicoQuant). The arrival time of every detected photon was recorded with a HydraHarp 400 counting module (PicoQuant).

FRET efficiency and intramolecular distances. Fluorescence bursts from individual molecules were identified by combining successive photons separated by inter-photon times of less than 150 μs and retaining the burst only if the total number of photons detected after donor excitation was greater than 40. Transfer efficiencies for each burst were calculated according to $E=n_A/(n_A+n_D)$, where n_D and n_A are the numbers of donor and acceptor photons, respectively, corrected for background, acceptor direct excitation, channel crosstalk, differences in detector efficiencies, and quantum yields of the dyes [11]. The histogram of transfer efficiencies was fitted with two empirical peak functions, using a normal distribution for both the donor-only and the FRET populations. Mean values of transfer efficiency $\langle E \rangle$ corresponding to the unfolded population were related to the distance information by solving numerically

$$\langle E \rangle = \int E(r)P(r)dr \quad \text{(eq. S10)}$$

for which we assumed for $P(r)$ the distance distribution of a random walk (Gaussian) chain,

$$P(r) = 4\pi r^2 \left(\frac{3}{2\pi R^2}\right)^{3/2} \exp(-\frac{3r^2}{2R^2}) \quad \text{(eq. S11a)}$$

where *R* is the root-mean-squared distance between the dyes. The mean distance inferred in this way was robust to the choice of polymer models to within 6 % when distance distributions for a worm-like chain[12]

$$P_{WLC}(r) = Z \frac{4\pi(r/l_c)^2}{l_c[1-(r/l_c)^2]^{9/2}} \exp(\frac{-3l_c}{4l_p[1-(r/l_c)^2]}) \quad \text{(eq. S11b)}$$

or an excluded volume chain[13]

$$P_{SAW}(r) = 4\pi r^2 \frac{0.278}{R^3} (\frac{r}{R})^{0.28} \exp(-1.206(\frac{r}{R})^{2.43}) \quad \text{(eq. S11c)}$$

were used (l_c is the contour length of the chain and *Z* is a normalization factor). Note that the distribution of transfer efficiency observed for the peak in the histogram (Figure S3) is dominated by shot noise, because the dynamics of inter-dye distance fluctuations is faster than the average interphoton time, and can thus not be used to infer a distance distribution directly [14]. Finally, to account for the length of dye linkers and compare the experimental data with simulations, *R* was rescaled to the distance between residues *m* and *n* according to

$$R_{m,n} = R \frac{|m-n|^{0.5}}{|m-n+2l|^{0.5}} \quad \text{(eq. S12)}$$

with *l* = 4.5 corresponding to the effective number of amino acid residues equivalent to one of the dyes with its linker [15].

Reconfiguration times from FRET-FCS. Autocorrelation curves of acceptor and donor channels and cross-correlation curves between acceptor and donor channels were computed from the measurements and analyzed as described previously [16]. The data were fitted over different time windows, from 1 μs to 5 μs (to assess the robustness of the fit), according to

$$g_{ij}(\tau) = 1 + \frac{1}{N}\left(1 - c_{AB}e^{-\frac{t-t_0}{\tau_{AB}}}\right)\left(1 + c_{CD}e^{-\frac{t-t_0}{\tau_{CD}}}\right)\left(1 + c_T e^{-\frac{t-t_0}{\tau_T}}\right) \quad \text{(eq. S13a)}$$

and

$$g_{ij}(\tau) = 1 + \left(\frac{f}{N}\left(1 + c_{CD}e^{-\frac{t-t_0}{\tau_{CD}}}\right) + \frac{1-f}{N}\left(1 + c_{CD2}e^{-\frac{t-t_0}{\tau_{CD2}}}\right)\right)\left(1 - c_{AB}e^{-\frac{t-t_0}{\tau_{AB}}}\right)\left(1 + c_{T}e^{-\frac{t-t_0}{\tau_{T}}}\right),$$

$$i, j = A, D \qquad \text{(eq. S13b)}$$

where *N* is the mean number of molecules in the confocal volume, c_{AB}, c_{CD}, c_{CD2} and c_T are the amplitudes related to photon antibunching (AB), chain dynamics (CD) and triplet blinking of the dyes (T), τ_{AB}, τ_{CD}, τ_{CD2} and τ_T are the corresponding relaxation times, f is the fraction of protein associated with the relaxation time τ_{CD} (for simplicity, brightness of the two fractions was considered to be identical). The relaxation times were extracted by fitting the three curves globally to eq. S13, assuming the same values of τ_{CD} but distinct triplet times for the three correlations. Assuming that chain dynamics can be described as a diffusive process in the potential of mean force derived from the sampled distance distribution $P(r)$ [17], we convert τ_{CD} and τ_{CD2} to the reconfiguration time of the chain, τ_r [16a]. Note that τ_{CD} and τ_r differ by only 6% in the present case because the root-mean-square distance is close to the Förster radius [16a].

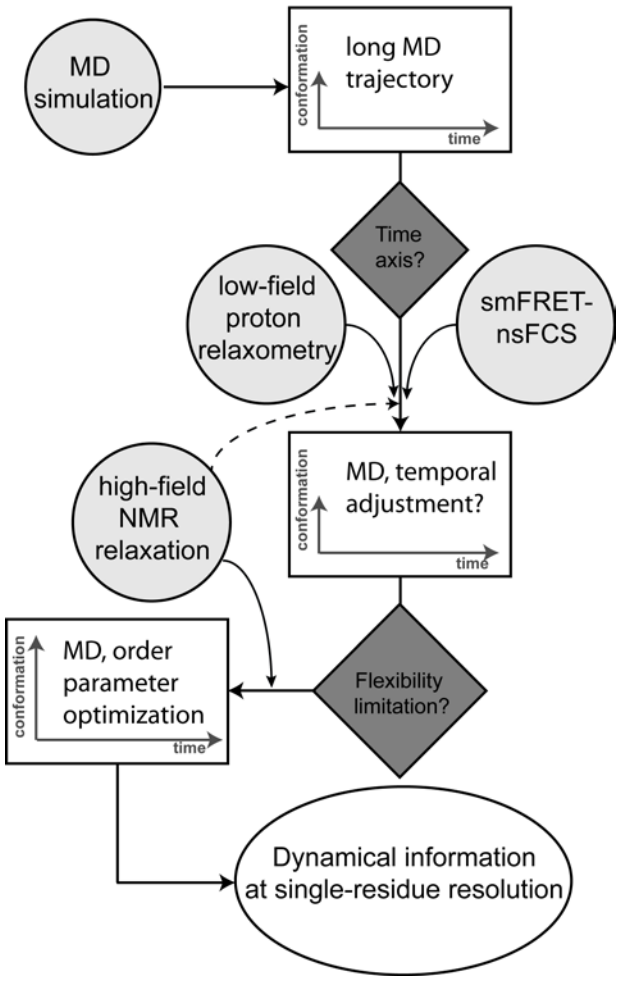

Figure S1. Flowchart representation of the approach of this study for investigating IDP dynamics through combination of MD simulation, low-field proton relaxometry, single-molecule FRET-nsFCS and high-field ^{15}N spin relaxation. It starts with a long MD simulation of the IDP of interest with the optimized force-field and water models. The duration of the MD simulation should be at least several microseconds to converge the longest dynamics expected for the IDP. Then, a careful analysis of experimental and simulated proton relaxometry profiles will provide correlation times of reorientational motions, and thus a global time axis scaling factor for the MD trajectory. The temporal adjustment of the MD trajectory can be further supported by single-molecule FRET-nsFCS data, which reprot chain reconfiguration dynamics in tens to hundreds of nanoseconds. Following temporal adjustment of the MD trajectory, high-field ^{15}N relaxation rates will be employed to detect local flexibility limitations in MD and optimizing order parameters at single-residue level. The approach of this study may be called "IASMIN", for the Integrative Approach for Scaling of Molecular dynamic simulation for Intrinsically disordered proteiNs.

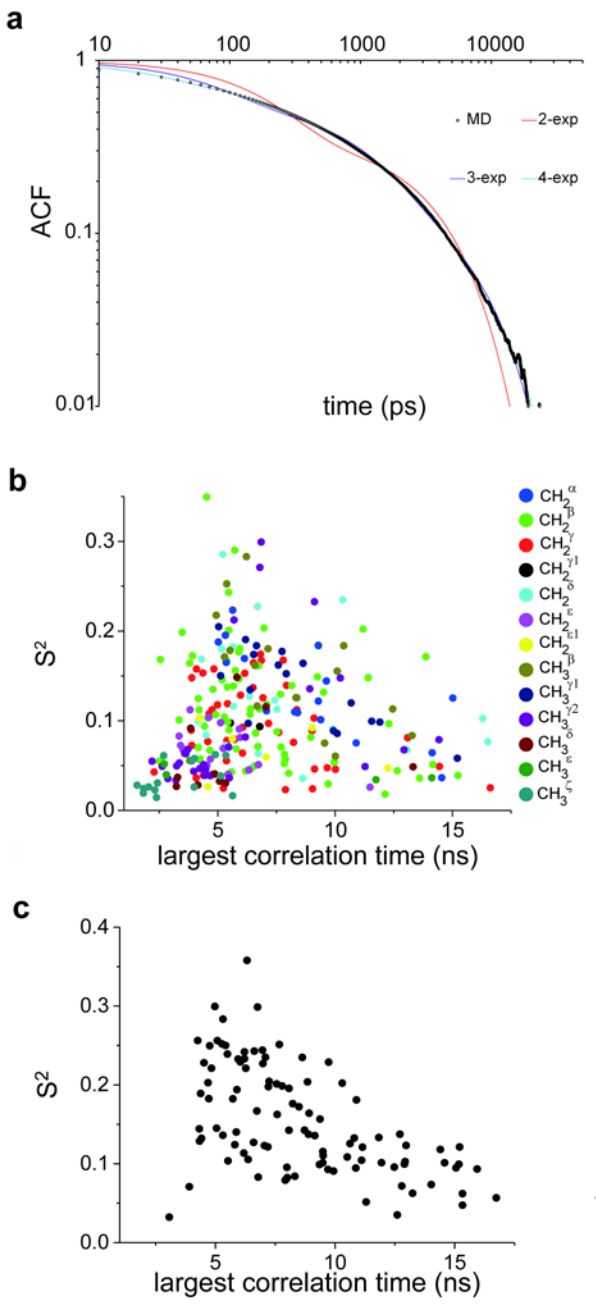

Figure S2. MD-based proton-proton angular autocorrelation functions (ACF). (a) The ACF of a representative H-H pair (gray circles), and its best-fit curves to two-, three- or four-exponential decay functions (solid lines). The decaying behavior of the ACF during the first 1000 ps is satisfactorily captured only when four exponential terms are included. (b,c) Longest correlation times and corresponding squared order parameters obtained from the fit of the MD-based ACFs of methylene and methyl protons (b) and CH^{α} protons (c). A large spread of correlation times and order parameters is observed over protein protons.

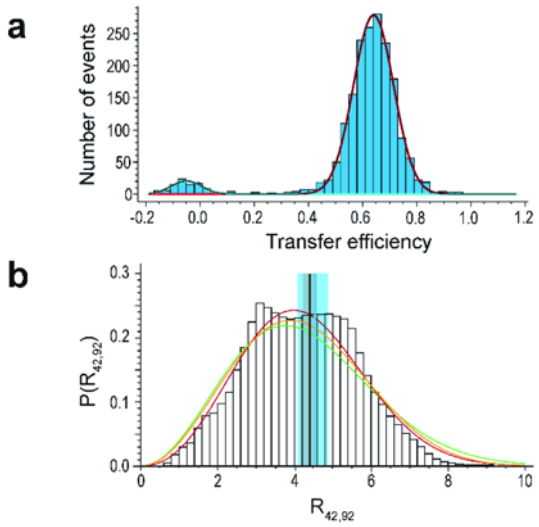

Figure S3. Single-molecule FRET of double-labeled S42C/T92C α-synuclein. (a) FRET efficiency histogram. The mean value of the transfer efficiency is 0.64, corresponding to an inter-dye distance of 4.7±0.2, 5.0±0.2, and 4.6±0.2 nm assuming a Gaussian, wormlike or a self-avoiding random walk, respectively. The small peak at zero FRET efficiency is due to molecules without active acceptor fluorophore. (b) Distance distributions of simple polymer models approximate the shape of the probability distribution for the C^{α}-C^{α} distance between residues 42 and 92 obtained from the MD simulation. The resulting root-mean-square-distances are: 4.6 nm (fit to Gaussian chain, green), 4.5 nm (fit to wormlike chain, orange), and 4.4 nm (fit to self-avoiding random walk, red). The root-mean-square distance calculated from the simulation data is 4.4±0.2 (black vertical line and gray shaded area). The corresponding experimental values are reported for comparison (cyan vertical line and shaded area).

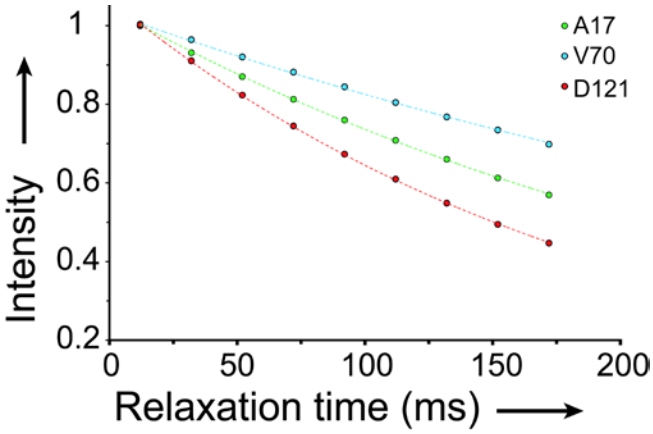

Figure S4. Experimental determination of ^{15}N relaxation rates. As typical examples, the intensity decay of three residues from the N-terminal, NAC and C-terminal regions (A17, V70 and D121, highlighted in Fig. 1d) in R_2 experiments are shown.

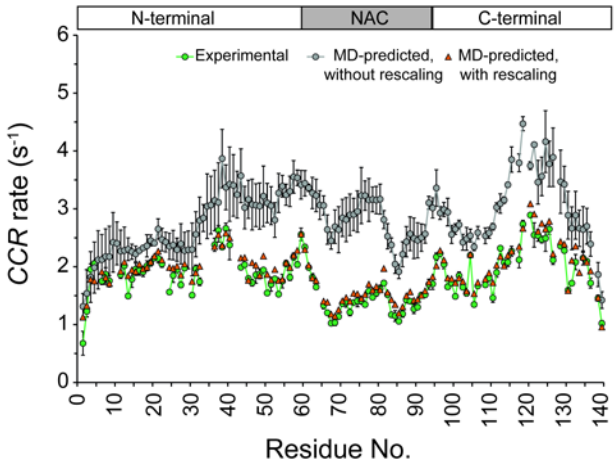

Figure S5. Residue-specific cross-correlated relaxation (*CCR*) rate between ^{1}H,^{15}N dipole-dipole and ^{15}N chemical shift anisotropy relaxation of α-synuclein, measured at 600 MHz proton Larmor frequency and 25 °C (green circles/lines). The rates calculated from the 16-μs MD trajectory are shown as gray circles, with the error bars representing the standard deviation between the rates calculated from three MD sub-trajectories, each of 5 μs duration. The predicted rates after rescaling of the MD are shown as orange triangles.

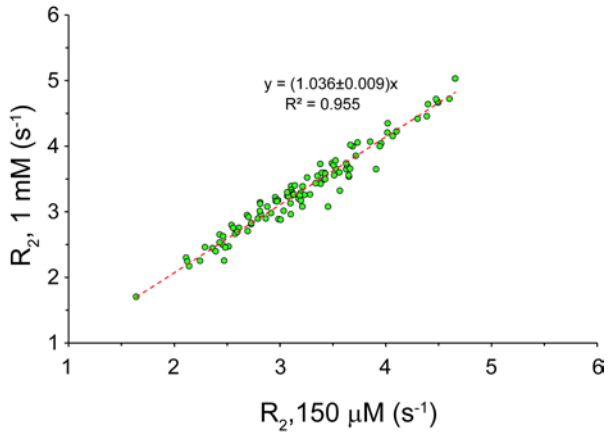

Figure S6. Comparison of ^{15}N R_2 relaxation rates of α-synuclein, measured at two different protein concentrations (1 mM and 150 μM). The ^{15}N relaxation rate measurements were performed at 800 MHz proton Larmor frequency and 25 °C. Since highly similar relaxation rates are obtained at these two protein concentrations, the possibility that α-synuclein aggregation makes a significant contribution to ^{15}N relaxation rates is excluded. The linear slope of 1.027-1.045 (95% CI) can be explained by the higher viscosity of the 1 mM α-synuclein sample, compared to the more dilute 150 μM sample. If we approximate that the R_2 is determined exclusively by $J(0)$ and ignore the small contributions from higher frequency terms, then an intrinsic viscosity of 2.21-3.69 cm^3/g (95% CI) would be required to explain the observed ratio of R_2 at two concentrations. The estimated value of intrinsic viscosity for α-synuclein is comparable to the intrinsic viscosities obtained for a broad range of proteins [18].

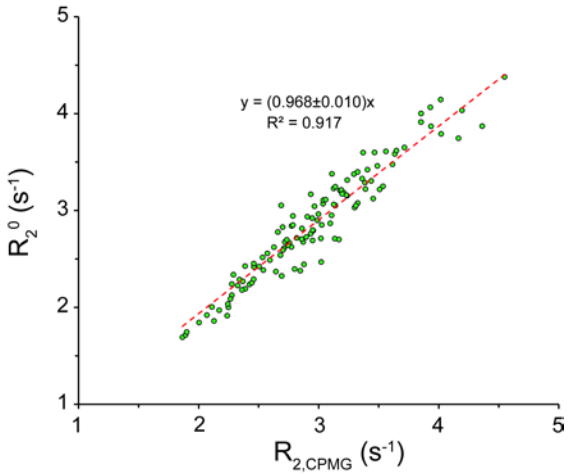

Figure S7. The exchange-free R_2 rates (R_2^0) calculated from *CCR* rates are in close agreement with the R_2 rates used for spectral density analysis, indicating that the deviation from single-Lorentzian behavior (shown in Figure S8) is unlikely to be caused by exchange contributions to relaxation rates. The reported slope represents 95% CI.

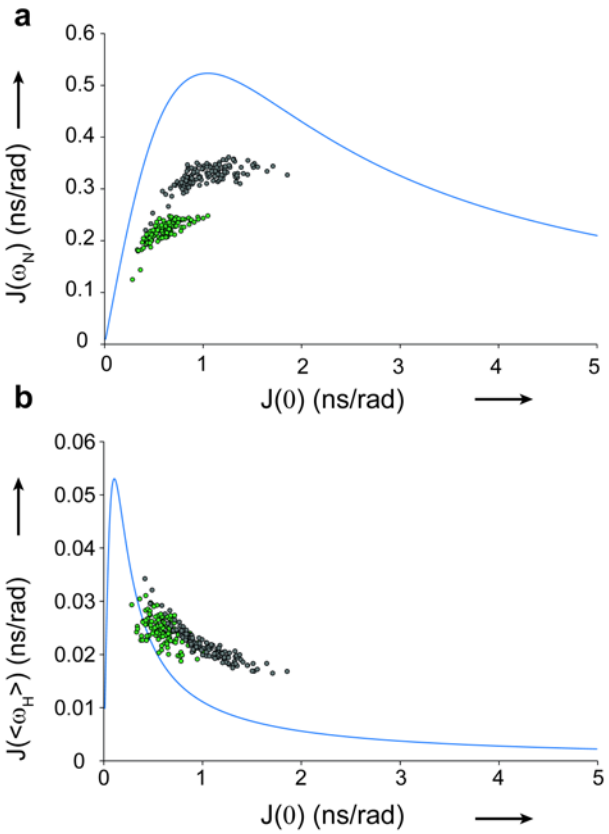

Figure S8. Spectral density analysis of experimental ^{15}N relaxation rates, shown here as $J(0)$ dependence of $J(\omega_N)$ (a, green circles) or $J(\langle\omega_H\rangle)$ (b, green circles), indicates that fast dynamics of α-synuclein backbone cannot be described by single-Lorentzian motions, i.e. motions with a single correlation time (blue curve). The MD-derived spectral density functions are shown by gray circles. The comparison between experimental (green circles) and simulated (gray circles) spectral density functions point to a general overestimation of $J(0)$ and $J(\omega_N)$ by MD.

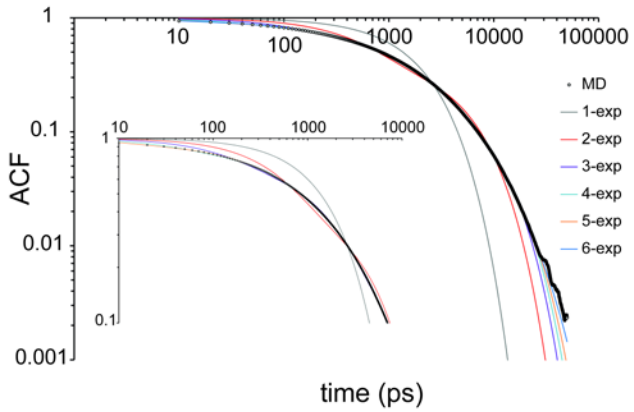

Figure S9. The global angular autocorrelation function (ACF) of N-H groups calculated from the MD trajectory (gray circles), fitted to a multi-exponential function with 1 to 6 exponential terms (solid lines). Successive addition of the exponential terms led to significant improvement in the quality of fit (P-value <0.0001), however inclusion of only three exponential terms was sufficient to lower the deviation between the simulation and fitted ACFs below the noise level in ACF. As a result, in accord with recent studies of IDP dynamics at multiple fields [19] and temperatures [20], we decided to fit residue-specific ACFs with three-exponential decay functions. As shown in the Inset, the fit in the first 100 ps of the ACF is sub-optimal when less than four exponential terms are included in the model. The MD-derived ACF exhibits some irregularities following ~ 30 ns, therefore only the initial 30 ns of the ACF were used for fitting.

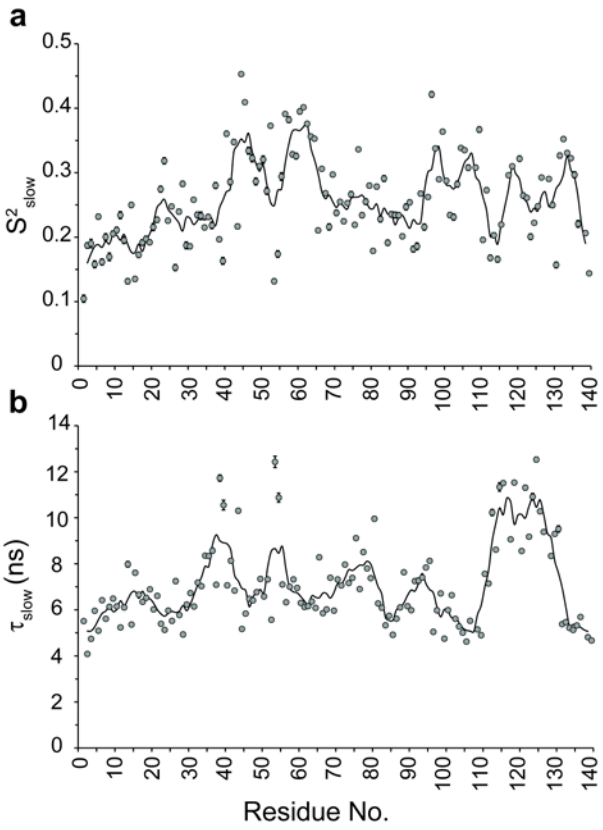

Figure S10. MD-based squared order parameters, S^2_{slow} (a), and correlation times, τ_{slow} (b), obtained from the fitting of angular autocorrelation functions of individual N-H vectors to a three-exponential decay function. Error bars, representing 95% CI, are mostly smaller than the symbol size. The solid lines show averaged values over a five-residue window.

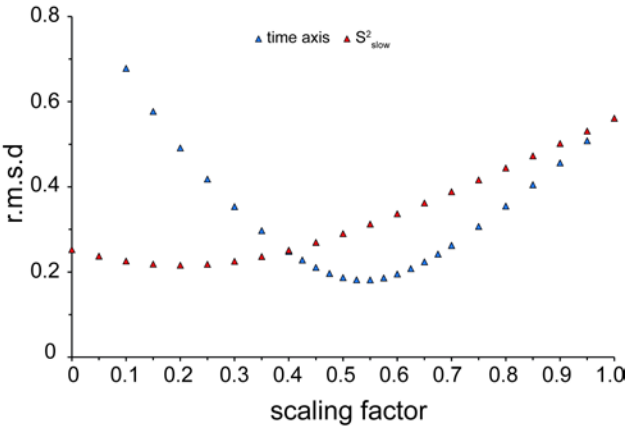

Figure S11. Dependence of the quality of fit between experimental and MD-predicted ^{15}N relaxation rates (R_1, R_2 and CCR at 600 MHz and R_2 at 800 MHz) on the global time axis (blue triangle) or S^2_{slow} (red triangle) rescaling of the MD trajectory. The best agreement between experimental and MD-predicted rates could be achieved after temporal adjustment by a factor of 0.55 or S^2_{slow} scaling of 0.20. For S^2_{slow} rescaling, the MD-based S^2_{slow} was multiplied by the specified scaling factor, then the order parameters of fast (S^2_{fast}) and intermediate (S^2_{int}) motions were accordingly re-scaled to keep $\sum S_i^2 = 1$ (i=1,2,3 for fast, intermediate and slow motions). The r.m.s.d was calculated as $rmsd = sqrt[(\left(\frac{R_{1,pred}-R_{1,exp}}{R_{1,exp}}\right))^2 + \left(\frac{R_{2,pred}-R_{2,exp}}{R_{2,exp}}\right))^2 + \left(\frac{CCR_{pred}-CCR_{exp}}{CCR_{exp}}\right))^2 + \left(\frac{R_{2,800,pred}-R_{2,800,exp}}{R_{2,800,exp}}\right))^2/4]$.

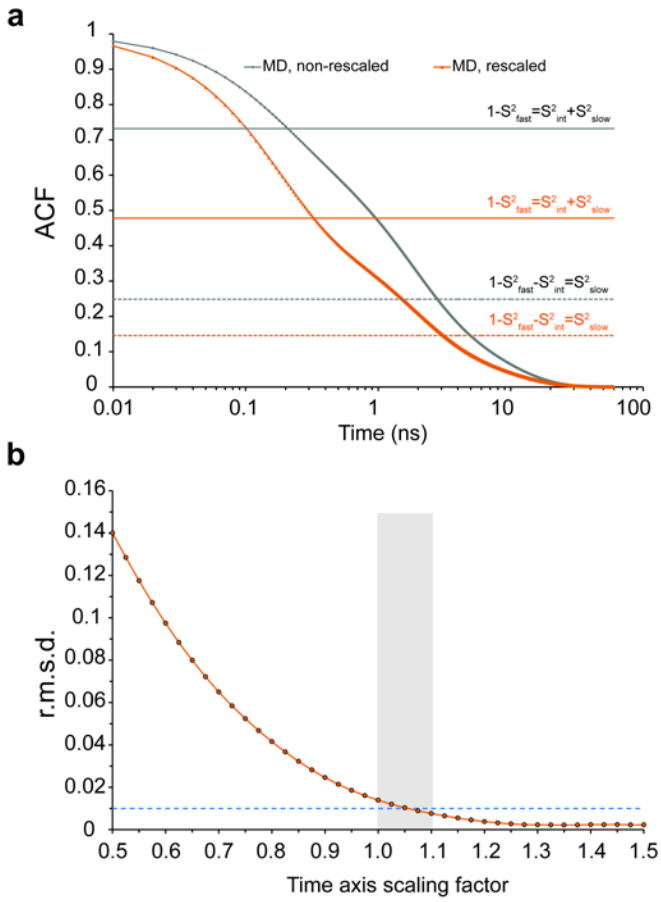

Figure S12. Optimization of MD-derived order parameters on the basis of ^{15}N relaxation rates, R_1 and R_2 at 600 MHz. (a) The best agreement with the experimental ^{15}N relaxation rates could be achieved through global time axis rescaling of the MD trajectory and optimization of the MD-derived order parameters. The average N-H autocorrelation function (ACF) is shown before (gray curve) and after (orange curve) such rescaling. The gray lines demonstrate how much of the N-H orientational memory remains in the MD-derived average ACF after fast (solid line) and intermediate (dotted line) motions are completed. The orange lines show the corresponding levels after rescaling of the average ACF. (b) Dependence of the quality of fit on the global time axis rescaling of the MD trajectory, while the order parameters are accordingly optimized. An excellent agreement could be achieved with time axis scaling factors at or above 1.05. In line with the proton relaxometry and nsFCS data, a time scaling factor of 1.05± 0.05 was used during order parameter optimization (shaded area).

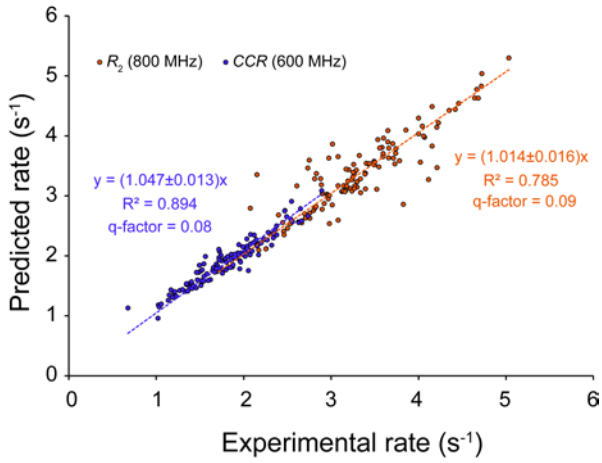

Figure S13. Cross-validation of optimized MD-based order parameters by $R_{2,800MHz}$ (orange circles) and CCR_{600MHz} (purple circles) rates. The predicted rates fit reasonably well to the experimental values.

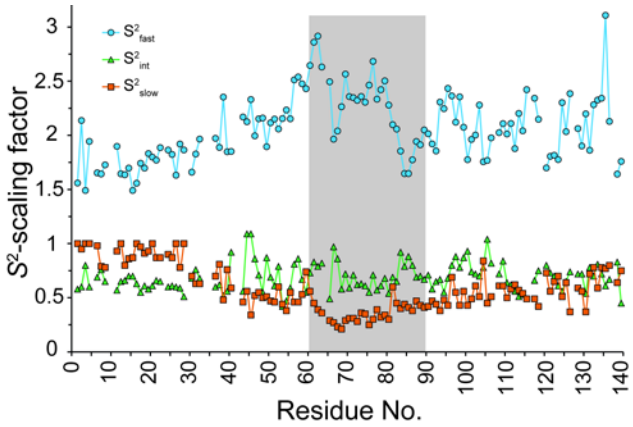

Figure S14. Degree of order parameter rescaling along α-synuclein sequence, reflecting the extent of local flexibility limitation in the MD trajectory. As indicated by the sequence dependence of S^2_{slow} scaling factor, the NAC region (shaded area) exhibit severe conformational sampling limitation, while the N-terminal residues 1-30 are least affected.

Table S1. Comparison of average intramolecular distances from single-molecule FRET and MD simulation

	$R_{42,92}$ (nm)			
	single-molecule FRET	MD simulation[a]	MD simulation best fit[b]	MD simulation from computed E[c]
Rms distance	-	4.4±0.2		
Gaussian chain	4.7±0.2	-	4.6	4.71
WLC[d]	4.6±0.2	-	4.5	5.06
SAW[e]	4.4±0.2	-	4.4	4.46

[a] Mean and standard deviation estimated by subdividing the simulation in 5 μs segments. [b] Root-mean-squared distance estimated from the best fit of the different polymer models to the simulated distance distribution. [c] Root-mean-squared distance estimated with the different polymer models from the mean transfer efficiency computed from the simulated data. [d] Worm-like chain. [e] Self-avoiding random walk chain

Table S2. Fitting of the MD-derived global N-H angular autocorrelation function (ACF) of α-synuclein to multi-exponential decay functions with up to six exponential terms

	τ_1[a] (S^2_1)	τ_2 (S^2_2)	τ_3 (S^2_3)	τ_4 (S^2_4)	τ_5 (S^2_5)	τ_6 (S^2_6)	SSE[b]
1-exp	1962±28	-	-	-	-	-	7.5160
	(1)						
2-exp	544±9	5122±51	-	-	-	-	0.3864
	(0.57)	(0.43)					
3-exp	152±3	1545±16	7321±51	-	-	-	0.0301
	(0.27)	(0.48)	(0.25)				
4-exp	41±1	512±6	2332±20	8666±45	-	-	0.0036
	(0.13)	(0.29)	(0.41)	(0.18)			
5-exp	13±0	211±3	1001±11	3321±32	10130±63	-	0.0005
	(0.08)	(0.17)	(0.32)	(0.32)	(0.12)		
6-exp	7±0	100±1	466±5	1619±15	4980±62	13635±238	<0.0001
	(0.05)	(0.09)	(0.21)	(0.34)	(0.25)	(0.06)	

[a] Correlation times (τ_i) in picosecond. 95% CIs are shown. The fitting error for squared order parameters (S^2_i, i=1 to 6) were generally <0.01. [b] Sum of Squared Errors. After successive inclusion of exponential terms from 1 to 6 terms, the quality of fit was significantly improved (P-value < 0.0001). Inclusion of only three exponential terms was sufficient to lower the deviation between the simulation and fitted ACFs below the noise level in ACF of 0.089. To evaluate the noise level in the ACF, the global ACFs were calculated for three non-overlapping MD sub-trajectories, each of 5 μs duration, and the average SSE between them and the average ACF was calculated.

Table S3. Overall comparison of experimental ^{15}N R_1 and R_2, ^{1}H,^{15}N heteronuclear NOE and *CCR* rates of α-synuclein with the rates predicted from the 16-μs MD trajectory of α-synuclein, calculated using Amber12 force field with sampling interval of 10 ps

		Experimental	MD-predicted	MD-predicted (time-rescaled) [b]	MD-predicted (S^2-rescaled)[c]
R_1	at 600 MHz (s^{-1}) [a]	1.39±0.10	1.62±0.07 (0.25)	1.59±0.14 (0.22)	1.75±0.17 (0.39)
R_2	at 600 MHz (s^{-1})	2.94±0.56	4.16±0.77 (1.38)	2.71±0.51 (0.51)	2.73±0.52 (0.52)
CCR	at 600 MHz (s^{-1})	1.81±0.42	2.83±0.56 (1.13)	1.78±0.37 (0.36)	1.78±0.37 (0.36)
hetNOE	at 600 MHz	-0.15±0.17	0.11±0.15 (0.29)	-0.10±0.22 (0.20)	-0.02±0.17 (0.21)
R_2	at 800 MHz (s^{-1})	3.30±0.64	5.00±0.95 (1.89)	3.05±0.60 (0.58)	3.07±0.58 (0.59)

[a] Errors are standard deviation of the experimental and MD-predicted rates over α-synuclein residues. In parentheses, the r.m.s.d. between experimental and MD-predicted rates are shown. [b] The time axis of the MD trajectory was rescaled by multiplying to 0.55. [c] The MD-based order parameter of the slow motion (S^2_{slow}) was multiplied by 0.20, then the order parameters of the fast (S^2_{fast}) and intermediate (S^2_{inter}) motions were accordingly re-scaled to keep $\sum S_i^2 = 1$.

References

[1] S. Piana, A. G. Donchev, P. Robustelli, D. E. Shaw, *J Phys Chem B* **2015**, *119*, 5113-5123.

[2] Y. E. Ryabov, D. Fushman, *J Am Chem Soc* **2007**, *129*, 3315-3327.

[3] G. Parigi, N. Rezaei-Ghaleh, A. Giachetti, S. Becker, C. Fernandez, M. Blackledge, C. Griesinger, M. Zweckstetter, C. Luchinat, *J Am Chem Soc* **2014**, *136*, 16201-16209.

[4] B. A. Borgias, P. D. Thomas, T. L. James, *Abstr Pap Am Chem S* **1989**.

[5] D. A. Case, *J Biomol NMR* **1999**, *15*, 95-102.

[6] P. Kaderavek, V. Zapletal, A. Rabatinova, L. Krasny, V. Sklenar, L. Zidek, *J Biomol NMR* **2014**, *58*, 193-207.

[7] A. G. Palmer, 3rd, *Annu Rev Biophys Biomol Struct* **2001**, *30*, 129-155.

[8] N. Tjandra, A. Szabo, A. Bax, *J Am Chem Soc* **1996**, *118*, 6986-6991.

[9] N. Rezaei-Ghaleh, K. Giller, S. Becker, M. Zweckstetter, *Biophys J* **2011**, *101*, 1202-1211.

[10] N. A. Farrow, O. Zhang, J. D. Forman-Kay, L. E. Kay, *Biochemistry* **1995**, *34*, 868-878.

[11] B. Schuler, S. Muller-Spath, A. Soranno, D. Nettels, *Methods Mol Biol* **2012**, *896*, 21-45.

[12] E. P. O'Brien, G. Morrison, B. R. Brooks, D. Thirumalai, *J Chem Phys* **2009**, *130*, 124903.

[13] A. V. Dobrynin, M. Rubinstein, *J Physique II* **1995**, *5*, 677-695.

[14] B. Schuler, H. Hofmann, A. Soranno, D. Nettels, *Annu Rev Biophys* **2016**, *45*, 207-231.

[15] aA. Hoffmann, A. Kane, D. Nettels, D. E. Hertzog, P. Baumgartel, J. Lengefeld, G. Reichardt, D. A. Horsley, R. Seckler, O. Bakajin, B. Schuler, *Proc Natl Acad Sci U S A* **2007**, *104*, 105-110; bM. Aznauryan, L. Delgado, A. Soranno, D. Nettels, J. R. Huang, A. M. Labhardt, S. Grzesiek, B. Schuler, *Proc Natl Acad Sci U S A* **2016**, *113*, E5389-5398.

[16] aI. V. Gopich, D. Nettels, B. Schuler, A. Szabo, *J Chem Phys* **2009**, *131*, 095102; bA. Soranno, B. Buchli, D. Nettels, R. R. Cheng, S. Muller-Spath, S. H. Pfeil, A. Hoffmann, E. A. Lipman, D. E. Makarov, B. Schuler, *Proc Natl Acad Sci U S A* **2012**, *109*, 17800-17806.

[17] D. Nettels, I. V. Gopich, A. Hoffmann, B. Schuler, *Proc Natl Acad Sci U S A* **2007**, *104*, 2655-2660.

[18] D. K. Hahn, S. R. Aragon, *J Chem Theory Comput* **2006**, *2*, 1416-1428.

[19] M. L. Gill, R. A. Byrd, A. G. Palmer, III, *Phys Chem Chem Phys* **2016**, *18*, 5839-5849.

[20] A. Abyzov, N. Salvi, R. Schneider, D. Maurin, R. W. Ruigrok, M. R. Jensen, M. Blackledge, *J Am Chem Soc* **2016**, *138*, 6240-6251.